Angewandte Chemie
Eine Zeitschrift der Gesellschaft Deutscher Chemiker

Supporting Information

69451 Weinheim, Germany

Activation of Oxygen on Gold and Silver Nanoparticles Assisted by Surface Plasmon Resonances**

Yi-Fan Huang, Meng Zhang, Liu-Bin Zhao, Jia-Min Feng, De-Yin Wu, Bin Ren,* and Zhong-Qun Tian*

anie_201310097_sm_miscellaneous_information.pdf

Supporting Information

Table of Content

S1. Dark-field characterization and position of Au film/PATP/Au NPs junctions

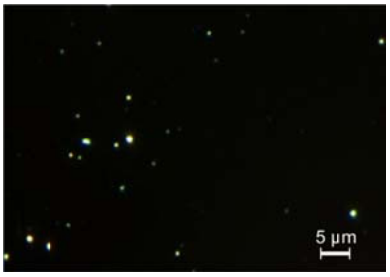

Figure S1 Dark field microscopic image of Au film/PATP/Au NPs junctions

The metal/molecule/metal NPs junctions can be precisely positioned via the light scattered by nanoparticles which could be efficiently observed by a dark field microscope.[1] As shown in Figure S1, the bright spots can be ascribed to the Au nanoparticles in the junctions.

S2. Comparative Raman spectra of Au film/PATP/Ag NPs and Ag film/PATP/Au NPs junctions in air and nitrogen atmosphere

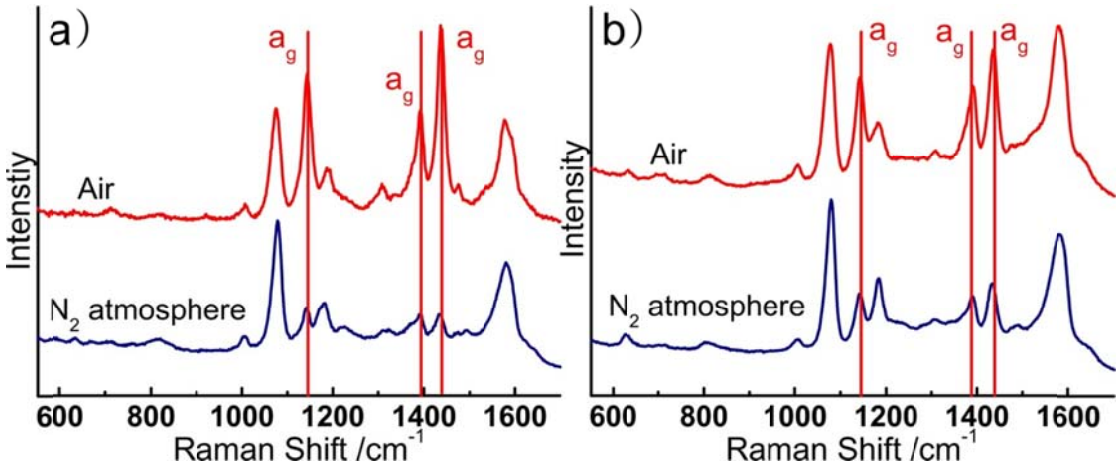

Figure S2 Raman spectra of Ag film/PATP/Au NPs (a) and Au film/PATP/Ag NPs (b) junctions recorded in air and the N_2 atmosphere

S3. DFT calculations on thermodynamic and kinetic energies of the oxidation of PATP

S3.1. Methods and Models

In the main text, we have experimentally demonstrated the Au or Ag oxide/hydroxide generated from oxygen gas ($^3O_2$) in air activated by SPR could selectively and rapidly oxidize PATP to DMAB. Conversely, in order to sensitively indicate the activation of oxygen gas ($^3O_2$) via the characteristic bands of DMAB, we herein performed DFT calculations to demonstrate that the transformation of PATP to DMAB is highly efficient and selective.

At the beginning, we tested our model to verify the calculation precision. The transformation of PATP to DMAB in SERS could be generally described by Equation S1. Because $^3O_2$ is involved in the open-shell calculation, we employed annihilated wave function to describe it in order to decrease the possible spin contaminant. As listed in Table S1, the oxidation is thermodynamically favorable, irrespective of the methods and annihilated wave functions. Therefore, we calculated the $^3O_2$ with normal wave function in the following.

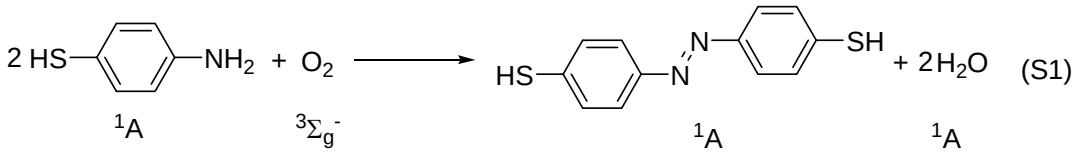

Table S1 Thermodynamic energy change of Equation S1 calculated by various methods

Methods	Thermodynamic Energy / kcal/mol		
	ΔE	ΔH	ΔG
B3LYP/6-311+G**	−52.45	−52.45	−51.53
PW91PW91/6-311+G**	−55.34	−53.78	−52.01
MP2/6-311+G**	−66.66	−64.72	−63.97
B3LYP/6-311+G**(Annihilation)	−52.46	−52.46	−51.53
G3MP2(Annihilation)	−63.56	−63.56	−63.09
G4MP2(Annihilation)	−63.67	−63.67	−62.34

Annihilation: the wave function of oxygen gas with an electronic state of $^3\Sigma_g^-$ is annihilated in order to decrease the possible spin contaminant.

In the SERS study, the SERS spectra are contributed by PATP adsorbed on Au or Ag nanoparticles. Because the transformation of PATP to DMAB focuses on the oxidation of amino group, we firstly performed a charge distribution study of the amino group of the PATP adsorbed on Au and Ag clusters via thiol group. As shown in Table S2, the Mulliken charge distributions of the amino group of PATP bonded to Au and Ag clusters are almost identical to that of free PATP. Hence, for the sake of calculation time, we only calculated the thermodynamic/kinetic energies of free PATP in the transformation to DMAB.

Table S2 Mulliken charge of the amino group in aromatic anilines and PATP bonded with Au and Ag clusters.

Species	Mulliken Charge Distribution /a.u.		
	N	H	H
NH_2-C_6H_4-SH	−0.359	0.227	0.227
NH_2-C_6H_4-SAu_3 (top site)	−0.359	0.228	0.229
NH_2-C_6H_4-SAg_3 (top site)	−0.366	0.221	0.221

NH_2-C_6H_4-SAu_5 (bridge site)	−0.360	0.230	0.229
NH_2-C_6H_4-SAg_5 (bridge site)	−0.363	0.225	0.224

S3.2. Temperature dependent thermodynamics of the oxidation of PATP

As discussed in the main text, the local temperature on the surface of nanoparticles may be greatly different from the room temperature in the presence of SPR. Table S3 presents the electronic energy change, the enthalpy change, and Gibbs free energy change of Equation S1 at temperatures ranging from 298.15 K to 600 K. The Gibbs free energy change is over −60 kcal/mol in this temperature range. Therefore, it can be finally concluded that the oxidation of PATP is thermodynamic favorable.

Table S3 Thermodynamic energy change of the oxidation of PATP by $^3O_2$ (Equation S1)

Temperature / K	Thermodynamic Energy / kcal/mol		
	ΔE	ΔH	ΔG
298.15	−63.67	−63.67	−62.34
300	−63.67	−63.67	−62.33
350	−63.51	−63.51	−62.12
400	−63.38	−63.38	−61.93
450	−63.27	−63.27	−61.76
500	−63.18	−63.18	−61.59
550	−63.11	−63.11	−61.44
600	−63.05	−63.05	−61.29

S3.3. Kinetics of the oxidation of PATP

The above thermodynamic energy change does not include any exact reaction pathway. We could not conclude the catalytic effects in the real experiments, including the selectivity and the activation energy. Therefore, we performed a quantitative study of the kinetic energy of the pathways according to the above experiments. The possible reaction pathways are proposed in Figure S3. To manifest the role of metals, we also calculated the kinetic energy of the reaction in the absence of metal, as shown in Figure S3a. Because not every product or intermediate has been experimentally characterized, we selected the species in each step according to the lowest total Gibbs free energy. For example, the total energy of the system involved in radical intermediates is lower than that of their anion/cation species. The pathway via the formation of the radical intermediates is also consistent with the conclusion in

literatures.[2]

The SERS experiments in the main text indicate Au or Ag oxide/hydroxide on the surface of Au or Ag nanoparticles is the precursor of the oxidation of PATP in the catalytic reaction. To avoid the complication in studying the oxide/hydroxide on the surface, we simplify the reaction system with a simple Ag_2O/AgOH, as shown in Figure S3b and c. It is interesting to find that the oxidation via the Au or Ag oxide/hydroxide is involved in nitrene-Ag_n or Au_n compounds instead of the radical intermediates. In this case, the selectivity is extremely high as has been observed in SERS experiments.

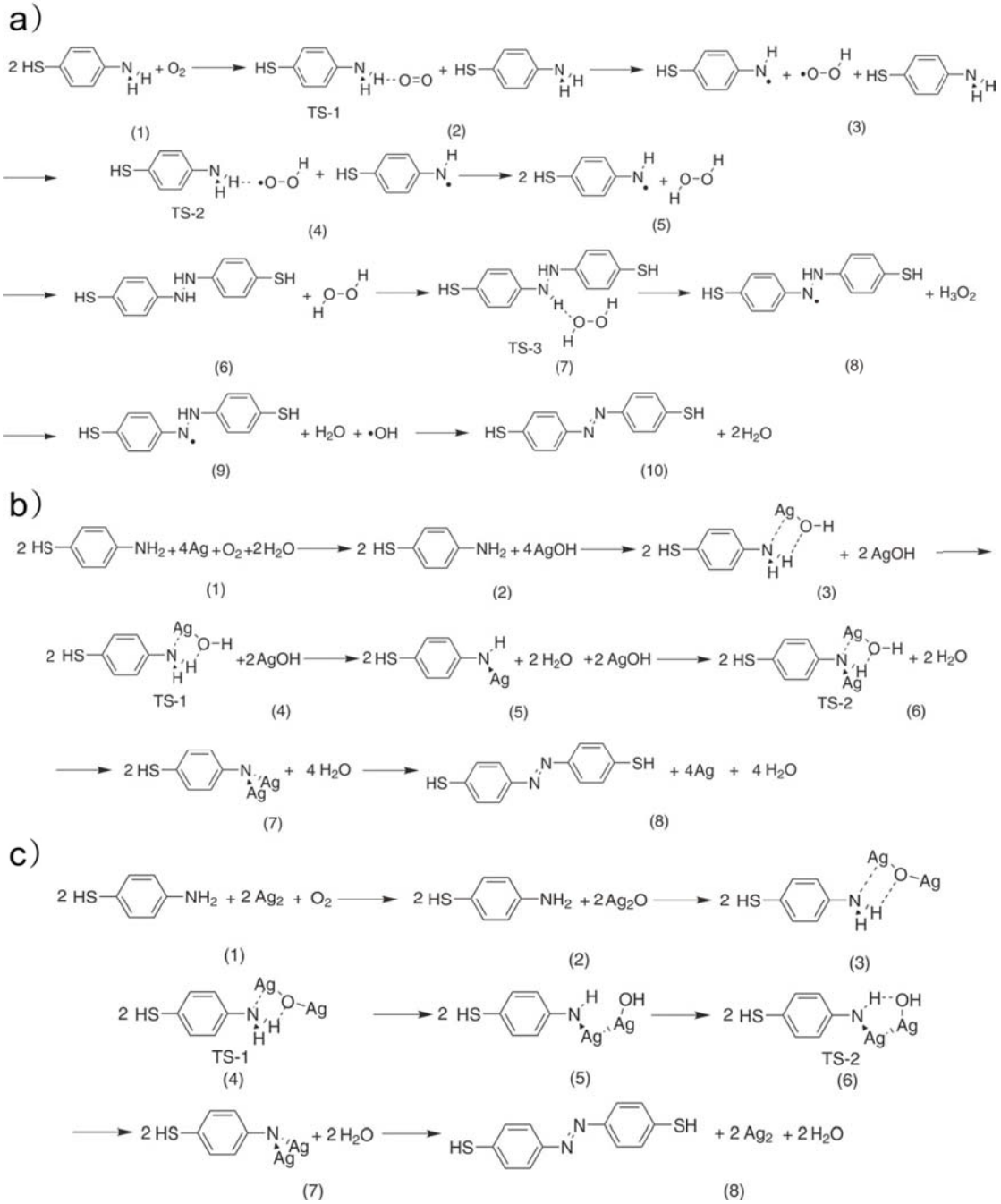

Figure S3 Reaction pathways of the oxidation of PATP by (a) $^3O_2$, (b) AgOH, and (c) Ag_2O

The estimation of activation energy will allow a quantitative estimation of the catalytic effect. We calculated the energy of the species involved in each elementary step for the above reaction pathway. Figure S4a and b show the Gibbs energy change of the oxidation by $^3O_2$ and Au and Ag oxide/hydroxide, respectively. Some successive endothermic steps can be found in both pathways. We estimated the activation energy by adding up the energy of the successive uphill steps, and the activation energies of these pathways are summarized in Table S4. It can be found that the rate-determined step for oxidation of PATP by $^3O_2$ is the first dehydrogen step and that by Au or Ag oxide/hydroxide is the second dehydrogen step. The final activation energy by $^3O_2$, AuOH, AgOH, Au_2O and Ag_2O are 33.4, 14.9, 7.3, 22.1 and 9.5 kcal/mol, respectively. It can be clearly seen that the activation energies are much lower in the presence of Au or Ag oxide/hydroxide, which should be the origin of the catalytic effect.

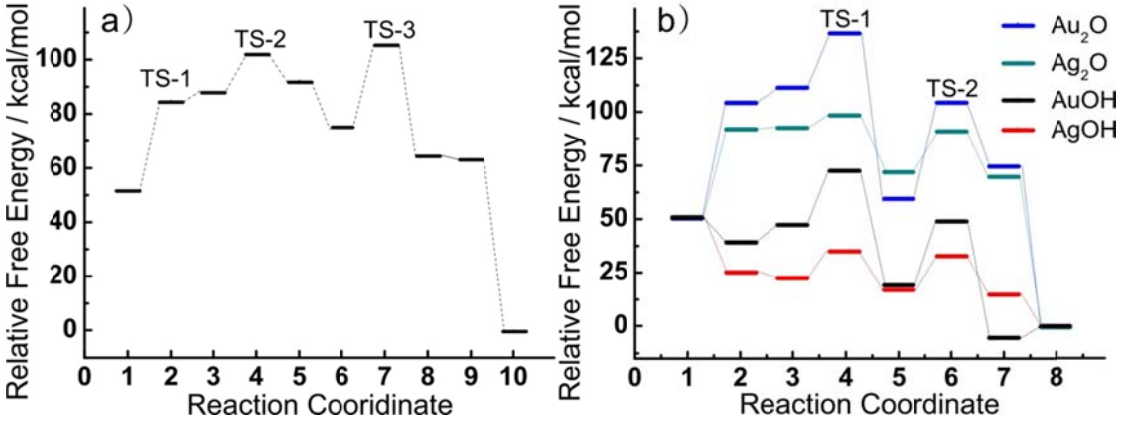

Figure S2 Energy curve of the oxidation of PATP by $^3O_2$ (a) and AgOH/Ag_2O (b)

Table S4 Kinetic energy change of the oxidation of PATP

Oxidation Reagent	Kinetics Energy / kcal/mol			
	E_{a1}	E_{a2}		
AuOH	12.6	14.9		
AgOH	6.1	7.3		
Au_2O	12.7	22.1		
Ag_2O	2.5	9.5		
$^3O_2$	E_{a1}	E_{a2}	E_{a3}	E_{a4}
	33.4	13.7	30.5	0.0

S4. Preparation of M/PATP/M NPs junctions and Raman measurements

S4.1. Synthesis of Au and Ag NPs and Au-core @ silica-shell (Au@SiO_2) NPs

The Au (ca. 55 nm in diameter) and Ag (ca. 80 nm in diameter) NPs were respectively synthesized by reducing the boiling 0.01 wt% $HAuCl_4$ and 1 mmol/L $AgNO_3$ solutions with 1 wt% sodium citrate under a vigorous stirring.[3] The Au-core @ silica-shell ($Au@SiO_2$) NPs were prepared by coating silica onto 55 nm Au NPs via the hydrolysis of sodium silicate in boiling water.[4]

S4.2. Preparation of M/PATP/M NPs junctions and SERS-active substrates

The Au (Ag)/PATP/Au (Ag) NPs junctions were constructed by assembling PATP and nanoparticles on Au or Ag flat film via a "layer-by-layer" procedure. A Au film, Ag film or Au(111) single crystal electrode was immersed into 1 mmol/L PATP ethanol solution for *ca.* 30 min. It should be emphasized that the **PATP ethanol solution should be freshly prepared**. Then, the films or Au(111) electrode were rinsed by ethanol. Afterwards, the films or Au(111) electrode were soaked in the above sols of Au or Ag for several minutes. At last, the films were rinsed by water and dried in vacuum.

In order to manifest the role of $^3O_2$, Raman measurements were performed in the atmosphere free of $^3O_2$. First, the films with constructed Au (Ag)/PATP/Au (Ag) NPs junctions were transferred into a gloves box filled with N_2, where the concentration of $^3O_2$ and H_2O is 0.4 and 0.01 ppm, respectively. Then, the film was placed within the space of two optically transparent quartz windows with a thickness of 0.5 mm. After that, the edge of the windows was strictly sealed by glue. At last, the films sealed within the windows were transferred into air for Raman measurements.

The comparative studies in HCl/H_2SO_4/NaOH solutions were performed on conventional SERS-active substrate. The Ag and Au sol were washed to remove the surfactant on the surface by alternately centrifuging the sol and filling pure water for 2 times. Then, the aggregates were dropped onto silicon wafers and dried in vacuum. After that, the wafers were immersed into 1 mmol/L PATP ethanol solution and soaked for *ca.* 30 min. Finally, they were rinsed by water and dried in vacuum.

S4.3. Raman measurements

The junctions were positioned according to the procedure in the S1 section and the

conventional measurements were carried out with a laser power of several milliwatts.

In the comparative studies in HCl, H_2SO_4, NaOH solutions, the solutions were prepared in air to allow sufficient almost of $^3O_2$ in air to be dissolved in the solutions. In the Raman measurement, these solutions were dropped onto the wafers covered with the SERS-active Au or Ag nanoparticles pre-adsorbed with PATP. Then, the samples were covered with a quartz window to form a closed system with essentially the same experimental condition for strict comparison. After that, the Raman spectra were acquired on the above samples.

S5. Apparatus

Raman spectra were obtained on XploRA (Jobin Yvon-Horiba, France) and Invia (Renishaw, UK) confocal Raman microscopes. Both of the Raman systems are integrated with dark field function. The two systems have a range of lasers of 532 nm (both), 638 nm (XploRA), 632.8 nm (Invia) and 785 nm (both). All the Raman measurements were performed on XploRA except the wavelength dependent experiment of Au/PATP/Au junctions on inVia.

The X-ray photoelectron spectroscopy (XPS) measurement was made in a vacuum chamber at a pressure less than 5×10^{-10} Torr on a Quantum 2000 spectrometer (PHI) equipped with an Al source.

S6. The Cartesian coordinates of some key species in calculations:

TS-1 in figure S1b

C	2.750953	1.261836	-0.119632
C	1.418031	1.602281	0.080681
C	0.453356	0.624192	0.385827
C	0.888235	-0.712180	0.483217
C	2.219047	-1.049416	0.279284
C	3.170854	-0.066447	-0.015122
H	3.473605	2.033343	-0.358265
H	1.113122	2.641162	-0.002513

H	0.166616	-1.488828	0.714694
H	2.528207	-2.085811	0.349162
H	-1.603674	0.302670	1.412010
S	4.883191	-0.514152	-0.349367
H	5.336043	-0.472318	0.923970
H	-1.027720	1.948837	0.631412
Ag	-2.632929	-0.161469	-0.537599
N	-0.887112	0.945098	0.591242
O	-2.629907	-0.319619	1.767706
H	-2.523400	-1.083902	2.340666

TS-2 in figure S1b

C	2.872605	0.572591	-0.976176
C	1.495265	0.639839	-0.835368
C	0.828179	0.049124	0.263392
C	1.641957	-0.612730	1.216288
C	3.021609	-0.682692	1.069325
C	3.659168	-0.083489	-0.020677
H	3.350305	1.032140	-1.834018
H	0.900679	1.155366	-1.584306
H	1.169982	-1.070934	2.078046
H	3.614486	-1.199274	1.815662
H	-1.109727	-0.615319	1.362325
S	5.442229	-0.215448	-0.230094
H	5.790678	0.926600	0.405501
Ag	-1.852264	-1.514932	-0.572294
N	-0.545135	0.063949	0.433663
O	-1.938651	-1.414825	1.814576
H	-1.552170	-2.089818	2.380045
Ag	-1.573851	1.874156	0.087300

TS-1 in figure S1c

C	3.974283	0.123876	1.127900
C	2.714392	0.529957	1.551940
C	1.563148	0.247499	0.790230
C	1.733945	-0.469328	-0.412630
C	2.995002	-0.866998	-0.833361
C	4.131993	-0.584022	-0.066725
H	4.845796	0.358986	1.728005
H	2.614512	1.081595	2.482106
H	0.855871	-0.702456	-1.005921
H	3.104516	-1.407000	-1.766933
H	-0.698813	0.051759	0.769825
S	5.773546	-1.038624	-0.651382
H	5.829279	-2.279728	-0.116766
H	0.258081	1.002385	2.128117
Ag	-1.077293	1.960335	-0.374358
N	0.296487	0.660005	1.175704
O	-1.735415	-0.084539	0.053176
Ag	-3.179189	-1.520276	0.046788

TS-2 in figure S1c

C	3.240696	1.123979	-0.116226
C	1.897274	1.222058	0.174878
C	1.105540	0.078008	0.501768
C	1.782477	-1.182543	0.465719
C	3.138642	-1.274031	0.212883
C	3.887311	-0.126623	-0.088320

H	3.807656	2.017830	-0.353698
H	1.413081	2.193549	0.170202
H	1.205408	-2.076127	0.674641
H	3.617607	-2.247315	0.226784
H	-0.714168	-1.066900	1.242019
S	5.622782	-0.169147	-0.460871
H	5.805200	-1.485665	-0.238161
N	-0.163064	0.153271	0.963863
O	-1.242286	-2.097824	1.236271
H	-1.673106	-2.274558	2.079034
Ag	-1.537440	1.543348	0.083293
Ag	-2.348902	-1.026111	-0.508151

S7. References

[1] T. Klar, M. Perner, S. Grosse, G. von Plessen, W. Spirkl, J. Feldmann, *Phys. Rev. Lett.* **1998**, *80*, 4249-4252.

[2] R. Konaka, K. Kuruma, S. Terabe, *J. Am. Chem. Soc.* **1968**, *90*, 1801-1806.

[3] G. Frens, *Nature Physical Science* **1973**, *241*, 20-22.

[4] J. F. Li, Y. F. Huang, Y. Ding, Z. L. Yang, S. B. Li, X. S. Zhou, F. R. Fan, W. Zhang, Z. Y. Zhou, D. Y. Wu, B. Ren, Z. L. Wang, Z. Q. Tian, *Nature* **2010**, *464*, 392-395.

M. J. Frisch, G. W. Trucks, H. B. Schlegel, G. E. Scuseria, M. A. Robb, J. R. Cheeseman, G. Scalmani, V. Barone, B. Mennucci, G. A. Petersson, H. Nakatsuji, M. Caricato, X. Li, H. P. Hratchian, A. F. Izmaylov, J. Bloino, G. Zheng, J. L. Sonnenberg, M. Hada, M. Ehara, K. Toyota, R. Fukuda, J. Hasegawa, M. Ishida, T. Nakajima, Y. Honda, O. Kitao, H. Nakai, T. Vreven, M. Jr., J. A. , J. E. Peralta, F. Ogliaro, M. Bearpark, J. J. Heyd, E. Brothers, K. N. Kudin, V. N. Staroverov, T. Keith, R. Kobayashi, J. Normand, K. Raghavachari, A. Rendell, J. C. Burant, S. S. Iyengar, J. Tomasi, M. Cossi, N. Rega, J. M. Millam, M. Klene, J. E. Knox, J. B. Cross, V. Bakken, C. Adamo, J. Jaramillo, R. Gomperts, R. E. Stratmann, O. Yazyev, A. J. Austin, R. Cammi, C. Pomelli, J. W. Ochterski, R. L. Martin, K. Morokuma, V. G. Zakrzewski, G. A. Voth, P. Salvador, J. J. Dannenberg, S. Dapprich, A. D. Daniels, O. Farkas, J. B. Foresman, J. V. Ortiz, J. Cioslowski, D. J. Fox, B.01 ed., Gaussian, Inc., Wallingford CT, 2009.